

A SYSTEMATIC STUDY OF THE THERMAL AND NONTHERMAL EMISSION IN THE SUPERNOVA REMNANT RCW 86 WITH SUZAKU

YOSHIO TSUBONE¹, MAKOTO SAWADA¹, AYA BAMBA^{1,2,3}, SATORU KATSUDA⁴, JACCO VINK⁵

ABSTRACT

Diffusive shock acceleration by the shockwaves in supernova remnants (SNRs) is widely accepted as the dominant source for Galactic cosmic rays. However, it is unknown what determines the maximum energy of accelerated particles. The surrounding environment could be one of the key parameters. The SNR RCW 86 shows both thermal and non-thermal X-ray emission with different spatial morphologies. These emission originate from the shock-heated plasma and accelerated electrons respectively, and their intensities reflect their density distributions. Thus, the remnant provides a suitable laboratory to test possible association between the acceleration efficiency and the environment. In this paper, we present results of spatially resolved spectroscopy of the entire remnant with Suzaku. The spatially-resolved spectra are well reproduced with a combination of a power-law for synchrotron emission and a two-component optically thin thermal plasma, corresponding to the shocked interstellar medium (ISM) with kT of 0.3–0.6 keV and Fe-dominated ejecta. It is discovered that the photon index of the nonthermal component becomes smaller with decreasing the emission measure of the shocked ISM, where the shock speed has remained high. This result implies that the maximum energy of accelerated electrons in RCW 86 is higher in the low-density and higher shock speed regions.

Subject headings: ISM: individual (RCW 86) — cosmic rays — supernova remnants — X-rays: ISM

1. INTRODUCTION

Cosmic rays are particles which bombard the Earth from anywhere (Hess 1912). X-ray and GeV/TeV γ -ray observations have revealed that the shocks of supernova remnants (SNRs) are the acceleration sites of the Galactic cosmic rays up to the TeV range (e.g., Koyama et al. 1995; Ackermann et al. 2013).

The diffusive shock acceleration mechanism (DSA; e.g. Malkov & Drury 2001) is believed to be the relevant mechanism, which can explain the power-law energy distribution. However it is still unclear what determines the efficiency. The surrounding environment should be one of the key parameters (Patnaude et al. 2009, for example). Typical X-ray spectra of SNRs show either synchrotron emission from high energy electrons, thermal emission from shock-heated interstellar medium (ISM), or combination of these. Therefore, by comparing spatial distributions of these emission, we may reveal association between the acceleration efficiency and the environment.

RCW 86 is a SNR located at (l, b) = (315.4, −2.5) with an apparent diameter of ~ 42 arcmin. The distance is estimated to be ~ 2.8 kpc (Rosado et al. 1996). Narayan et al. (1977) discovered the X-rays from RCW 86 for the first time. Because of the low plasma temperature (~ 0.5 keV), RCW 86 had been assumed to be an old remnant. However, since the detection of high temperature emission by Chandra and XMM-Newton, RCW 86 is accepted as the remnant of SN 185 (Vink et al. 2006). The average radio spectral index is 0.6 (Green 1988). Furthermore, the X-

ray spectra of the SNR show not only thermal X-rays but also synchrotron X-rays (Bamba et al. 2000; Borkowski et al. 2001), implying that this SNR is an electron accelerator up to \sim TeV range, together with gamma-ray detection from GeV to TeV band (Yang et al. 2014; Aharonian et al. 2009). In fact, evidence for effective cosmic-ray acceleration has been reported (Bamba et al. 2005; Helder et al. 2011, 2013), although Shimoda et al. (2015) suggested the measured efficiency could be higher than reality. It is noteworthy that the thermal and non-thermal emission in this SNR is not uniform and have different morphology, which makes this SNR a suitable laboratory to test a possible relation between the acceleration efficiency and the environment.

In this paper, we present the systematic analysis of spatially resolved spectra obtained with the X-ray Imaging Spectrometer (XIS; Koyama et al. 2007) onboard Suzaku (Mitsuda et al. 2007). Unless otherwise noted the uncertainty is given at the 90% confidence interval.

2. OBSERVATION AND DATA REDUCTION

The entire region of RCW 86 is covered by six observations with Suzaku. The observation log is summarized in table 1. The fields of views (FoVs) are shown in Fig. 1 with the dashed squares.

The XIS consists of four X-ray CCD cameras, which observes in 0.2–12.0 keV with X-ray telescopes (XRT; Serlemitsos et al. 2007). Three of them (XIS 0, 2, and 3) are front-illuminated (FI) CCDs, and the other (XIS 1) is a back-illuminated (BI) CCD. The FI CCDs have larger effective area in the hard X-ray band while the BI CCD in the soft band. A pre-flight energy resolution is ~ 130 eV (Full width at half maximum, FWHM) at 5.9 keV (Koyama et al. 2007). After 2006 November 9, the XIS 2 was out of operation. The others (XIS 0, 1, and 3) use spaced-row charge injection (SCI; Nakajima et al. 2008; Uchiyama et al. 2009) to recover the charge transfer efficiency and improving the energy resolution after 2006 October. Each XRT accumulates X-rays with the effective area of 250 cm² at 8.0 keV to make an image over an $18' \times 18'$ FoV with angular resolutions of $1'.9\text{--}2'.3$ in

¹ Department of Physics and Mathematics, Aoyama Gakuin University 5-10-1 Fuchinobe, Chuo-ku, Sagami-hara, Kanagawa 252-5258, Japan

² Department of Physics, The University of Tokyo, 7-3-1 Hongo, Bunkyo-ku, Tokyo 113-0033, Japan

³ Research Center for the Early Universe, School of Science, The University of Tokyo, 7-3-1 Hongo, Bunkyo-ku, Tokyo 113-0033, Japan

⁴ Department of Physics, Faculty of Science & Engineering, Chuo University, 1-13-27 Kasuga, Bunkyo-ku, Tokyo 112-8551, Japan

⁵ Anton Pannekoek Institute/GRAPPA, University of Amsterdam PO Box 94249, NL-1090 GE Amsterdam, the Netherlands

the half-power diameter. Thanks to the low-Earth orbit, the non-X-ray background (NXB) is fairly low and stable. Thus, Suzaku is very suitable for RCW 86, with its large extent and low surface brightness in some regions.

We reprocessed the data using the xispi software and the recent calibration database released on 2012 May 9. The data were reduced in accordance with the standard screening criteria⁶. Grades 0, 2, 3, 4, and 6 events were used in following analysis. We removed events during the South Atlantic Anomaly passages, Earth elevation angles below 5°, and Earth day-time elevation angles below 20°. We also removed hot and flickering pixels. The resultant systematic uncertainty in the energy gain is < 12 eV. The XIS was operated in the normal clocking mode and full-window mode in the all observations.

In this paper, we use the software packages HEASoft version 6.10 and XSPEC version 12.7.1 and AtomDB version 1.3.2. In the spectral analysis, we generated the redistribution matrix function and ancillary response file using xisrmfgen and xissimarfgen (Ishisaki et al. 2007), respectively.

3. RESULTS

3.1. Image

In Figure 1, we show the XIS images of RCW 86. Red and blue show the 0.5–2.0 keV and 3.0–5.5 keV band images, respectively. The soft band is dominated by the thermal emission, whereas the hard one is dominated by non-thermal emission. NXB events were generated by xisnxbgen (Tawa et al. 2008) and subtracted from the image. We corrected exposure and vignetting using the flat images at 1 keV (soft band) and 4 keV (hard band) generated by xissim (Ishisaki et al. 2007). Both of these images show similar shell-like structure. However, their distributions are not identical. They show offsets in the azimuthal direction. For example, in the southern half of the shell, the soft emission appears from west to southwest, while the hard emission from southwest to south. They also show difference in the radial distributions. The soft emission is sharper while the hard emission is broader and patchier. These results are consistent with previous observations (e.g., ASCA: Bamba et al. 2000; Borkowski et al. 2001, Chandra: Bamba et al. 2005; Rho et al. 2002; Castro et al. 2013, XMM-Newton: Vink et al. 2006; Broersen et al. 2014).

3.2. Spectral Analysis

As the image shows, the thermal and non-thermal emission have different spatial distribution. For the spatially-resolved spectroscopy we divided RCW 86 in regions and determined physical parameters using the following steps. First, we determined the parameters such as temperature for each FoV (see Section 3.2.1). Next, we subdivided the FoV in regions, and we fitted the spectra of these regions using the best-fit model for each FoV, but the normalization and power-law index were treated as free parameters (see Section 3.2.2). Generating the ARF file, we assume the 1.7–5.0 keV image as the brightness distribution. We used the spectral data of XIS-FI CCDs.

3.2.1. Integrated spectra in each FoV

We show the integrated spectra in each FoV in Fig. 2. These spectra have been corrected for NXB, using the spectra generated by xisnxbgen (Tawa et al. 2008).

Yamaguchi et al. (2008, 2011) showed that the emission in RCW 86 can be well reproduced by two temperature plasma and power-law component model, and taking into account Galactic absorption. The low-temperature component corresponds to the shock-heated ISM, and is modeled with the vpshock model. The high-temperature component corresponds to the heated ejecta and was modeled by the vnei model. Finally, the power-law component represents the synchrotron emission from accelerated electrons. In vnei, we fixed the temperature and the ionization timescales to 5 keV and $10^9 \text{ cm}^{-3} \text{ s}$, respectively, following Yamaguchi et al. (2011). Furthermore, the abundances were fixed to solar abundance except for iron, for which we set the abundance to 10^{10} solar under the assumption that the ejecta plasma consists only of Fe ions and electrons (Yamaguchi et al. 2011). Because of uncertainties in the model, we ignored the energy bands of 0.70–0.78 and 1.13–1.28 keV (Yamaguchi et al. 2011). In addition, the 1.83–1.85 keV range was ignored, as the instrument response is uncertain in this range.

Because of the differences of spectral shapes in SW (Bamba et al. 2000, Borkowski et al. 2001), we divided SW into SW-A and SW-B. SW-B contains SW 03, 04, 12, and 13 (see Figure 1). The others were included in SW-A. These regions are much brighter than other regions, thus we further included the following steps to reduce uncertainty of the responses. We applied a gaussian for Fe-K β line with the fixed central energy and the sigma of gaussian to 7.1 keV and 0 eV, respectively. The gaussian smoothing (gsmooth model in XSPEC), with a freely varying sigma at 6 keV and a fixed index of 0.5 to take account of the energy dependence, is also applied to mitigate residuals in the low-energy band likely due to calibration uncertainty in instrumental broadening. Furthermore, we treated the gain as a free parameter.

In the EAST, there are the residuals of the NXB subtraction. When we checked the spectra from each FI sensor, XIS 2 spectrum had more residuals than those of the other XISs, implying that the low reproducibility of NXB at XIS 2 causes these residuals. Therefore, we did not use the spectra of XIS 2 for the analysis of EAST region. When we fitted EAST spectrum in 0.5–7.0 keV, the best-fit parameters did not change significantly.

By the above-mentioned method, we obtained the reasonable fitting results in the all of FoV for complicated SNR emission. Table 2 and 3, and Figure 2 show the best-fit parameters and models. Although it is not perfect in some regions, the purpose of this paper is not to determine the thermal parameters but to measure general trends in the emission measure of the thermal emission and the properties of X-ray synchrotron emission. Therefore, we do not pursue this model furthermore.

3.2.2. Spectra in the divided regions

In the next step, we analyzed the spectra of the divided regions. The spectral parameters were fixed to those of each FoV region (Table 2 and 3), except for the normalization of each component and the power-law indices which were treated as free. We chose the background regions in each FoV, where there is no bright source nor a calibration source. For the WEST region, we used the background for SE since the FoV of the WEST region only covers regions with emission from the bright shell, without any obvious region from which to extract a background spectrum. We show the spectra and best-fit parameters Tables 4–10, respectively. The model fits

⁶ see (http://heasarc.nasa.gov/docs/suzaku/processing/criteria_xis.html)

were generally good given the small number of free parameters.

Our results can change with different AtomDB version. We thus compared the fitting with v1.3.2, 2.0.2, and 3.0.3. The largest difference is shown in the Fe L lines in the ISM component, and it makes the difference of best-fit emission measure with the factor of around 2. All the other components did not show significant change among different AtomDB versions. Since our aim is to examine rough characteristics of thermal emission, and the best-fit emission measure scatter to more than 4 orders of magnitude, we concluded that the difference of AtomDB version does not change our result significantly.

Table 4 to 10 show that SOUTH08 region has the hardest spectrum. We also fitted the spectrum in this region with *srcut* model (Reynolds & Keohane 1999) instead of the power-law model addition to thermal emission, in order to estimate the roll-off energy of synchrotron emission in this region. The index of *srcut* were fixed to 0.6 (Green 1988). As the χ^2/dof is 147/155, the fit is acceptable, and this model is slightly better than previous model with power-law. We obtained the roll-off energy $h\nu_{\text{rolloff}} = 0.61^{+0.11}_{-0.19}$ keV.

In Figure 4, 5, and 6, we show the spatial distributions of the the square root of the emission measure of the ISM heated plasma ($EM^{1/2}$), the surface brightness of the synchrotron emission (the SB_{NT}), and the photon indices, respectively. $EM^{1/2}$ is primarily proportional to the plasma density, whereas SB_{NT} is proportional to a combination of the density of the accelerated electrons, the magnetic field strength, and the maximum energy of the electrons in the region. Finally, the photon index of synchrotron emission has correlation with the maximum acceleration energy and/or magnetic field strength (e.g., Reynolds & Keohane 1999). Toward southwest to west $EM^{1/2}$ and photon index become larger, whereas SB_{NT} smaller. In the northeast and south regions, we have strong and hard synchrotron emission, and faint thermal emission. According to Figure 6, we find the spatial difference of the photon indices. Then we show the azimuthal dependence of photon indices in Figure 7. We set NORTH01 to 0° . The emission goes hard around 190° (south), and goes soft around 100° (southwest) and 260° (east). We fit it with the constant model and rejected with the χ^2/dof of 672.4/42. This result shows existence of azimuth angle dependence.

4. DISCUSSION

We have conducted the systematic spatially-resolved spectroscopy of RCW 86, and found that the spectral shape changes from region to region. Here, we discuss in which environment the synchrotron emission becomes brighter and/or harder.

Figure 8 (a) and (b) show photon indices and SB_{NT} as a function of $EM^{1/2}$ (an indicator of the plasma density). One can see that the photon index becomes smaller when $EM^{1/2}$ becomes smaller. The correlation coefficient is 0.38 ± 0.15 (1σ variance) ± 0.03 (1σ statistical), indicating a marginally positive correlation. It implies that the acceleration to the higher energy in the low density medium. The northeast and south regions are obvious cases with hard nonthermal emission and low ambient density, whereas the high density region, such as southwest and west, shows softer nonthermal emission. The northeast region is known to be an efficient acceleration site with high shock velocity (Helder et al. 2013; Yamaguchi et al. 2016), whereas the shock speed in southwest

and north is much smaller (Ghavamian et al. 2001; Katsuda 2014; Frascchetti et al. 2016; Long & Blair 1990; Castro et al. 2013). So our results show that the maximum energy of accelerated electrons is higher in high shock speed region. This agrees with Yamazaki et al. (2006) and Aharonian & Atoyan (1999), which suggest that the roll-off of synchrotron emission depends only on the shock velocity if the maximum electron energy is determined by the balance between accelerating and synchrotron cooling. In order for a more quantitative study of the dependence of the maximum energy on shock velocity, we need more precise shock velocity measurement for the entire remnant. The south region, which is very interesting region with the hardest spectrum and very low ambient density in this remnant. This region coincides with the void of H_I cloud (Sano et al. 2016), which is consistent with our scenario.

Figure 7 shows the complex azimuthal dependence of photon index. Azimuthal dependence is also reported in SN 1006 (Rothenflug et al. 2004; Miceli et al. 2009; Katsuda et al. 2010). SN 1006 has rather simple bipolar morphology, and such a dependence is believed to be due to the effect of the magnetic field parallel to the Galactic Plane (Petruk et al. 2009) with the polarization observations in the radio band (Reynoso et al. 2013). On the other hand, it is not rejected yet the effect of perpendicular magnetic field (Bamba et al. 2003), since Richtmyer-Meshkov instability can make radial magnetic field in young SNRs even if the background magnetic field is perpendicular on the shock (Inoue et al. 2013). The situation is not so simple in our case. The photon index is harder in the south region, but we have no bipolar trend. This result indicates the reason of the photon index change may not the global magnetic field configuration but the shock speed differences as shown before. This may be because RCW 86 is evolving inside a stellar wind bubble (Broersen et al. 2014); the stellar wind makes complicated shock evolution together with complex circumstellar medium structure.

On the other hand, we found no correlation between $EM^{1/2}$ and SB_{NT} as shown in Figure 8 (b), which showed that we have no clear connection between the background plasma density and the surface brightness of synchrotron emission. The surface brightness of synchrotron emission depends not only on the number density of accelerated particles but also the strength of magnetic field, which makes perhaps for a more complicated relation between synchrotron surface brightness and plasma density. It may also be that the magnetic field is turbulent on scales smaller than our region size. It will be needed to compare these parameters in smaller size regions with a better angular resolution.

These results may be connected with the fact that many TeV gamma-ray SNRs have no significant thermal X-rays and their plasma densities are believed to be very low. In practice, thermal emission is not found at a significant level in Vela Jr. (Slane et al. 2001), RX J1713.7–3946 (Takahashi et al. 2008)⁷, and HESS J1731–347 (Bamba et al. 2012). RCW 86 has shell-like TeV and GeV gamma-ray emission (Aharonian et al. 2009; Yang et al. 2014), in addition to the thermal and nonthermal X-rays. Given that RCW 86 has regions with thermal emission and regions resembling the overall emission characteristics of RX J1713.7–3946 and Vela Jr, it may be a key object to understand the gamma-ray

⁷ Recently, Katsuda et al. (2015) detected thermal X-rays with the ejecta origin from the center of RX J1713.7–3946, but we have no clue on interstellar medium surrounding this SNR yet.

TABLE 1
SUZAKU OBSERVATIONS OF RCW 86

Region	Observation ID	Start date yyyy/mm/dd	Exposure (ks)	R.A. (deg)	Decl. (deg)	# of XIS	SCI
SW	500004010	2006/02/12	100.8	220.28	-62.68	4	off
EAST	501037010	2006/08/12	59.8	221.26	-62.36	4	off
NORTH	503002010	2009/01/29	55.4	220.50	-62.21	3	on
SOUTH	503003010	2009/01/31	54.8	220.83	-62.67	3	on
SE	503004010	2009/02/01	53.5	221.39	-62.67	3	on
WEST	503001010	2009/02/02	53.6	220.28	-62.43	3	on

and X-ray synchrotron emission of these large TeV gamma-ray emitting shell-type SNRs. In the future, studies with the Cherenkov Telescope Array (CTA) (Actis et al. 2011; Acharya et al. 2013) will reveal us the detailed morphology of RCW 86 with better spatial resolution and sensitivity, allowing for more exploring in more detail correlations between the thermal and non-thermal X-ray emission and the gamma-ray emission.

We thank the anonymous referee for the fruitful comments. We also would like to thank R. Yamazaki, Y. Ohira, and J. Shimoda for their fruitful discussion. This work is supported in part by Grant-in-Aid for Scientific Research of the Japanese Ministry of Education, Culture, Sports, Science and Technology (MEXT) of Japan, No. 22684012 and 15K05107 (A. B.), 15K17657 (M. S.), and 16K17673 (S. K.).

Facilities: Suzaku

REFERENCES

- Acharya, B. S., Actis, M., Aghajani, T., et al. 2013, *Astroparticle Physics*, 43, 3
- Ackermann, M., Ajello, M., Allafort, A., et al. 2013, *Science*, 339, 807
- Actis, M., Agnetta, G., Aharonian, F., et al. 2011, *Experimental Astronomy*, 32, 193
- Aharonian, F. A., & Atoyan, A. M. 1999, *A&A*, 351, 330
- Aharonian, F., Akhperjanian, A. G., de Almeida, U. B., et al. 2009, *ApJ*, 692, 1500
- Bamba, A., Koyama, K., & Tomida, H. 2000, *PASJ*, 52, 1157
- Bamba, A., Yamazaki, R., Ueno, M., & Koyama, K. 2003, *ApJ*, 589, 827
- Bamba, A., Yamazaki, R., Yoshida, T., et al. 2005, *ApJ*, 621, 793
- Bamba, A., Pühlhofer, G., Acero, F., et al. 2012, *ApJ*, 756, 149
- Borkowski, K. J., Rho, J., Reynolds, S. P., & Dyer, K. K. 2001, *ApJ*, 550, 334
- Broersen, S., Chiotellis, A., Vink, J., & Bamba, A. 2014, *MNRAS*, 441, 3040
- Castro, D., Lopez, L. A., Slane, P. O., et al. 2013, *ApJ*, 779, 49
- Foster, A. R., Ji, L., Smith, R. K., & Brickhouse, N. S. 2012, *ApJ*, 756, 128
- Fraschetti et al. 2016, in prep.
- Ghavamian, P., Raymond, J., Smith, R. C., & Hartigan, P. 2001, *ApJ*, 547, 995
- Green, D. A. 1988, *Ap&SS*, 148, 3
- Inoue, T., Shimoda, J., Ohira, Y., & Yamazaki, R. 2013, *ApJ*, 772, L20
- Ishisaki, Y., Maeda, Y., Fujimoto, R., et al. 2007, *PASJ*, 59, 113
- Helder, E. A., Vink, J., & Bassa, C. G. 2011, *ApJ*, 737, 85
- Helder, E. A., Vink, J., Bamba, A., et al. 2013, *MNRAS*, 435, 910
- Hess V.F. 1912, *Phys. Zeits* 13, 1084
- Katsuda, S. 2014, 40th COSPAR Scientific Assembly, 40, 1426
- Katsuda, S., Petre, R., Mori, K., et al. 2010, *ApJ*, 723, 383
- Katsuda, S., Acero, F., Tominaga, N., et al. 2015, *ApJ*, 814, 29
- Koyama, K., Petre, R., Gotthelf, E. V., et al. 1995, *Nature*, 378, 255
- Koyama, K., Tsunemi, H., Dotani, T., et al. 2007, *PASJ*, 59, 23
- Long, K. S., & Blair, W. P. 1990, *ApJ*, 358, L13
- Malkov, M. A., & Drury, L. O. 2001, *Reports on Progress in Physics*, 64, 429
- Miceli, M., Bocchino, F., Iakubovskiy, D., et al. 2009, *A&A*, 501, 239
- Mitsuda, K., Bautz, M., Inoue, H., et al. 2007, *PASJ*, 59, 1
- Nakajima, H., Yamaguchi, H., Matsumoto, H., et al. 2008, *PASJ*, 60, 1
- Naranan, S., Shulman, S., Yentis, D., Fritz, G., & Friedman, H. 1977, *ApJL*, 213, L53
- Patnaude, D. J., Ellison, D. C., & Slane, P. 2009, *ApJ*, 696, 1956
- Petrak, O., Dubner, G., Castelletti, G., et al. 2009, *MNRAS*, 393, 1034
- Rho, J., Dyer, K. K., Borkowski, K. J., & Reynolds, S. P. 2002, *ApJ*, 581, 1116
- Reynolds, S. P., & Keohane, J. W. 1999, *ApJ*, 525, 368
- Reynoso, E. M., Hughes, J. P., & Moffett, D. A. 2013, *AJ*, 145, 104
- Rosado, M., Ambrocio-Cruz, P., Le Coarer, E., & Marcelin, M. 1996, *A&A*, 315, 243
- Rothenflug, R., Ballet, J., Dubner, G., et al. 2004, *A&A*, 425, 121
- Sano, H., Nakamura, K., Furukawa, N., et al. 2016, *arXiv:1606.07745*
- Serlemitsos, P. J., Soong, Y., Chan, K.-W., et al. 2007, *PASJ*, 59, 9
- Shimoda, J., Inoue, T., Ohira, Y., et al. 2015, *ApJ*, 803, 98
- Slane, P., Hughes, J. P., Edgar, R. J., et al. 2001, *ApJ*, 548, 814
- Tawa, N., Hayashida, K., Nagai, M., et al. 2008, *PASJ*, 60, 11
- Takahashi, T., Tanaka, T., Uchiyama, Y., et al. 2008, *PASJ*, 60, 131
- Uchiyama, H., Ozawa, M., Matsumoto, H., et al. 2009, *PASJ*, 61, 9
- Vink, J., Bleeker, J., van der Heyden, K., et al. 2006, *ApJ*, 648, L33
- Yamaguchi, H., Koyama, K., Nakajima, H., et al. 2008, *PASJ*, 60, 123
- Yamaguchi, H., Koyama, K., & Uchida, H. 2011, *PASJ*, 63, 837
- Yamaguchi, H., Katsuda, S., Castro, D., et al. 2016, *ApJ*, 820, L3
- Yamazaki, R., Kohri, K., Bamba, A., et al. 2006, *MNRAS*, 371, 1975
- Yang, R.-z., Zhang, X., Yuan, Q., & Liu, S. 2014, *A&A*, 567, AA23

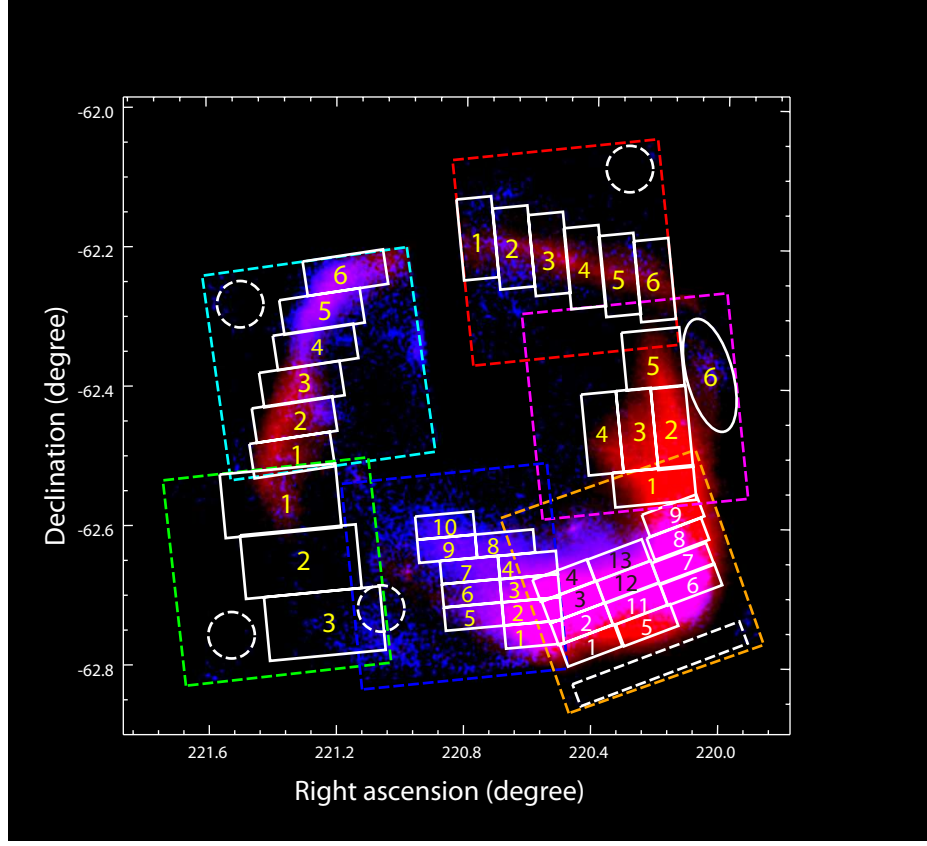


FIG. 1.— The XIS image of RCW 86 in a logarithmic scale. Red and blue respectively show emission from 0.5–2.0 keV (soft) and 3.0–5.5 keV (hard). The FoVs of XIS are indicated by the dashed squares. They are EAST (cyan), SE (green), SOUTH (blue), SW (orange), WEST (magenta) and NORTH (red). The solid-white shapes are source regions, while the dashed-white shapes are background regions in each FoV. The white and black numbers in the SW region represent SW-A and SW-B regions, as shown in the main text.

TABLE 2
THE BEST-FIT PARAMETERS FOR THE EACH FOV.

Parameter	EAST	NORTH	SE	SOUTH	WEST
–wabs–					
N_{H} (10^{21} cm^{-2})	3.3 ± 0.1	3.4 ± 0.1	2.1 ± 0.1	4.2 ± 0.1	3.3 ± 0.1
–vpshock–					
kT (keV)	0.44 ± 0.03	0.46 ± 0.02	0.59 ± 0.07	0.36 ± 0.02	0.46 ± 0.01
Ne (solar)	1.9 ± 0.1	1.8 ± 0.1	$2.4^{+0.2}_{-0.1}$	1.4 ± 0.1	1.8 ± 0.1
Mg (solar)	1.9 ± 0.2	1.3 ± 0.1	$2.0^{+0.4}_{-0.3}$	$0.96^{+0.16}_{-0.12}$	1.0 ± 0.1
Si (solar)	$1.9^{+0.6}_{-0.5}$	$1.8^{+0.4}_{-0.3}$	$3.2^{+1.3}_{-0.9}$	$1.2^{+0.5}_{-0.4}$	1.4 ± 0.1
Ca (solar)	1.2 ± 0.1	$0.73^{+0.07}_{-0.06}$	$1.1^{+0.2}_{-0.1}$	$0.93^{+0.09}_{-0.07}$	0.62 ± 0.02
τ ($10^{10} \text{ s cm}^{-3}$)	$3.2^{+0.9}_{-0.5}$	$3.2^{+0.6}_{-0.5}$	$2.5^{+1.0}_{-0.5}$	$9.1^{+2.6}_{-1.6}$	5.7 ± 0.4
Norm (10^{-16} cm^{-5})	1.14 ± 0.02	1.30 ± 0.02	0.218 ± 0.005	2.91 ± 0.04	4.28 ± 0.03
–power-law–					
Γ	2.72 ± 0.02	2.81 ± 0.02	2.49 ± 0.03	2.70 ± 0.01	2.86 ± 0.03
Norm ^a	1.30 ± 0.02	0.84 ± 0.02	0.43 ± 0.01	2.74 ± 0.03	0.70 ± 0.02
–vnei–					
Norm (10^{-21} cm^{-5})	4.6 ± 0.8	4.5 ± 0.7	2.9 ± 0.7	5.6 ± 1.0	6.9 ± 0.8
χ^2/dof	550/464	385/314	382/349	745/583	576/323

^a In unit of 10^{-2} photons $\text{keV}^{-1} \text{ s}^{-1} \text{ cm}^{-2}$ at 1 keV.

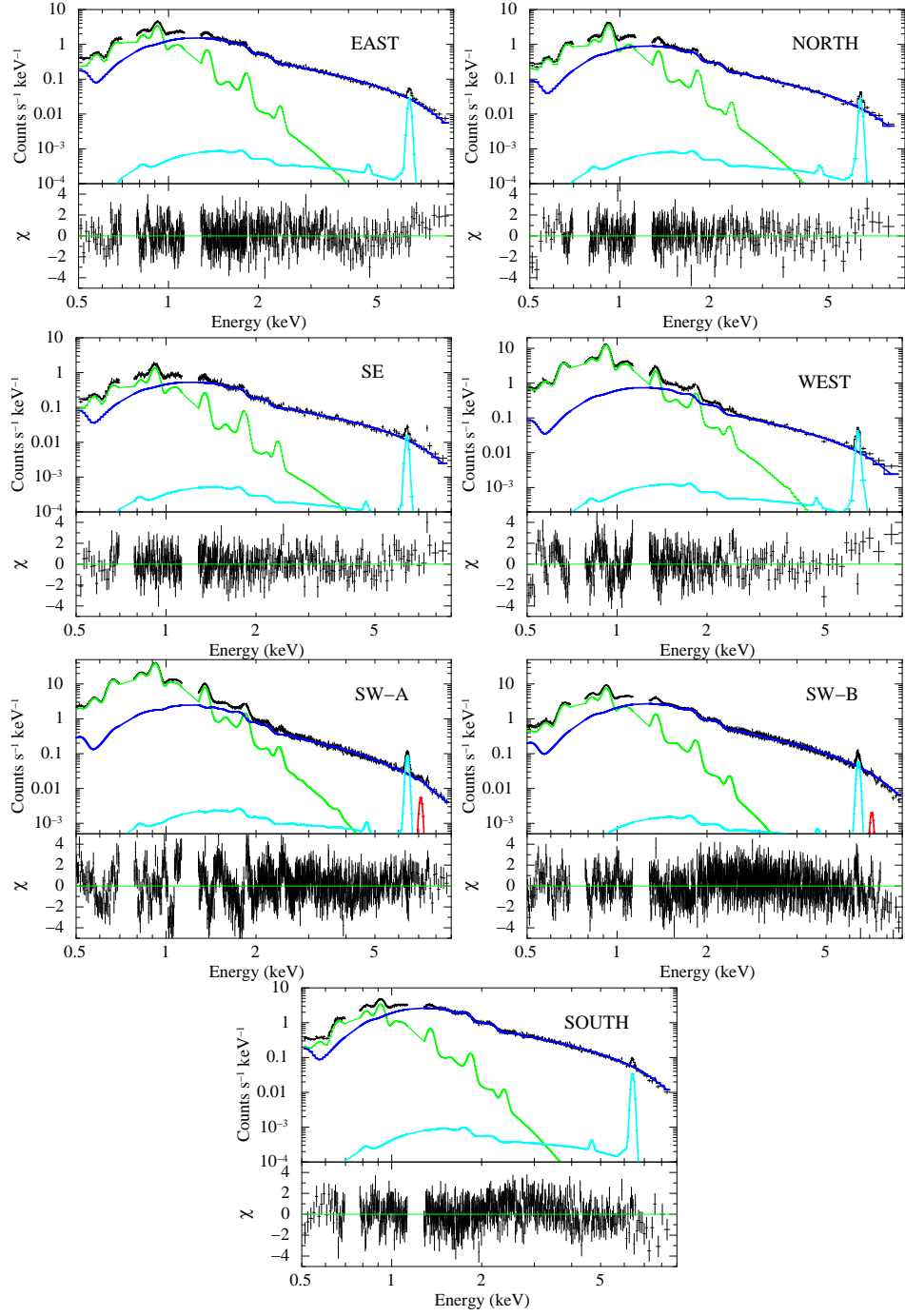


FIG. 2.— The Integrated spectra in each FoV. The blue, green, and cyan represents power-law, low-temperature plasma (vpshock), and high-temperature plasma (vnei) component. The red line of SW-A and SW-B are the gaussian indicated Fe-K β line.

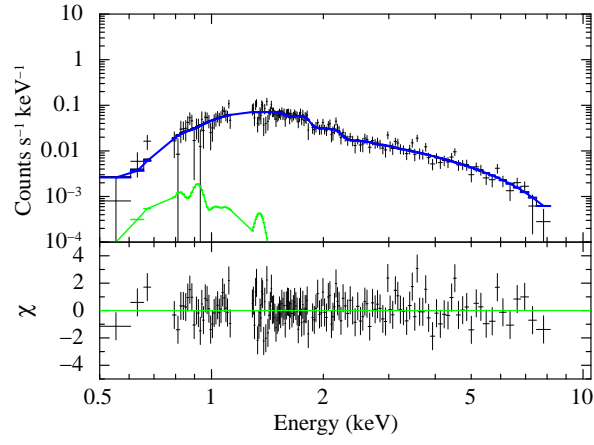


FIG. 3.— The SOUTH08 spectrum with with srcut fixed photon index and freed radio flux. The color is equivalent to Figure 2.

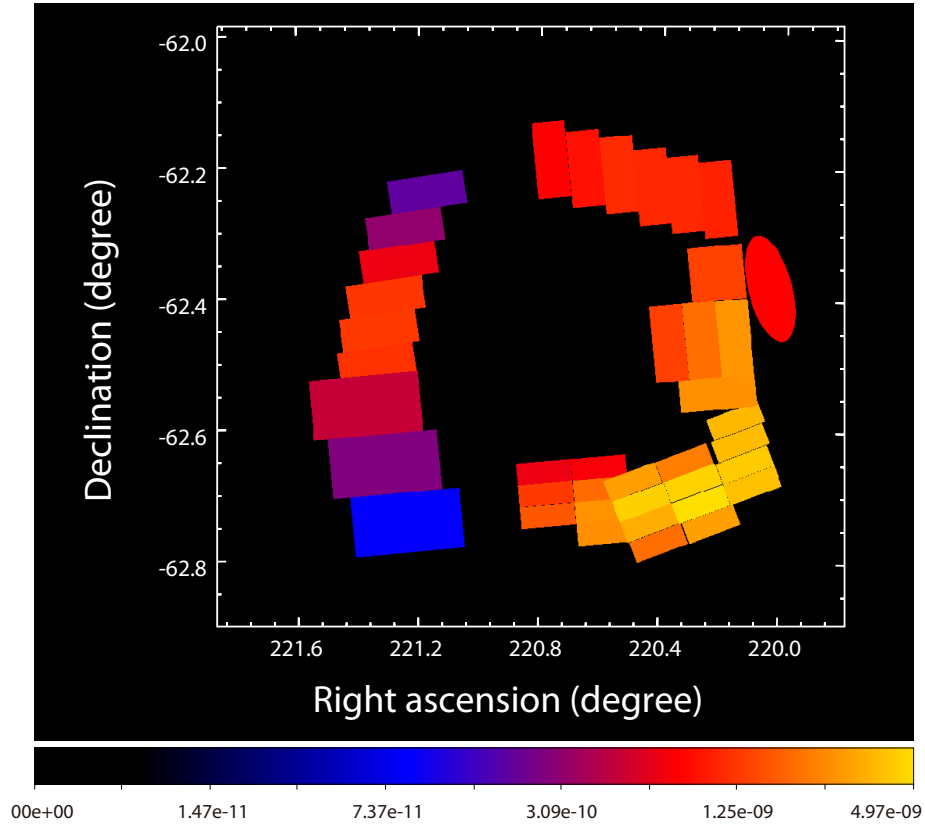


FIG. 4.— The $EM^{1/2}$ map. The scale is logarithmic. Note that SOUTH10 is invisible since this region has a very low $EM^{1/2}$ value near the lower limit of the color map.

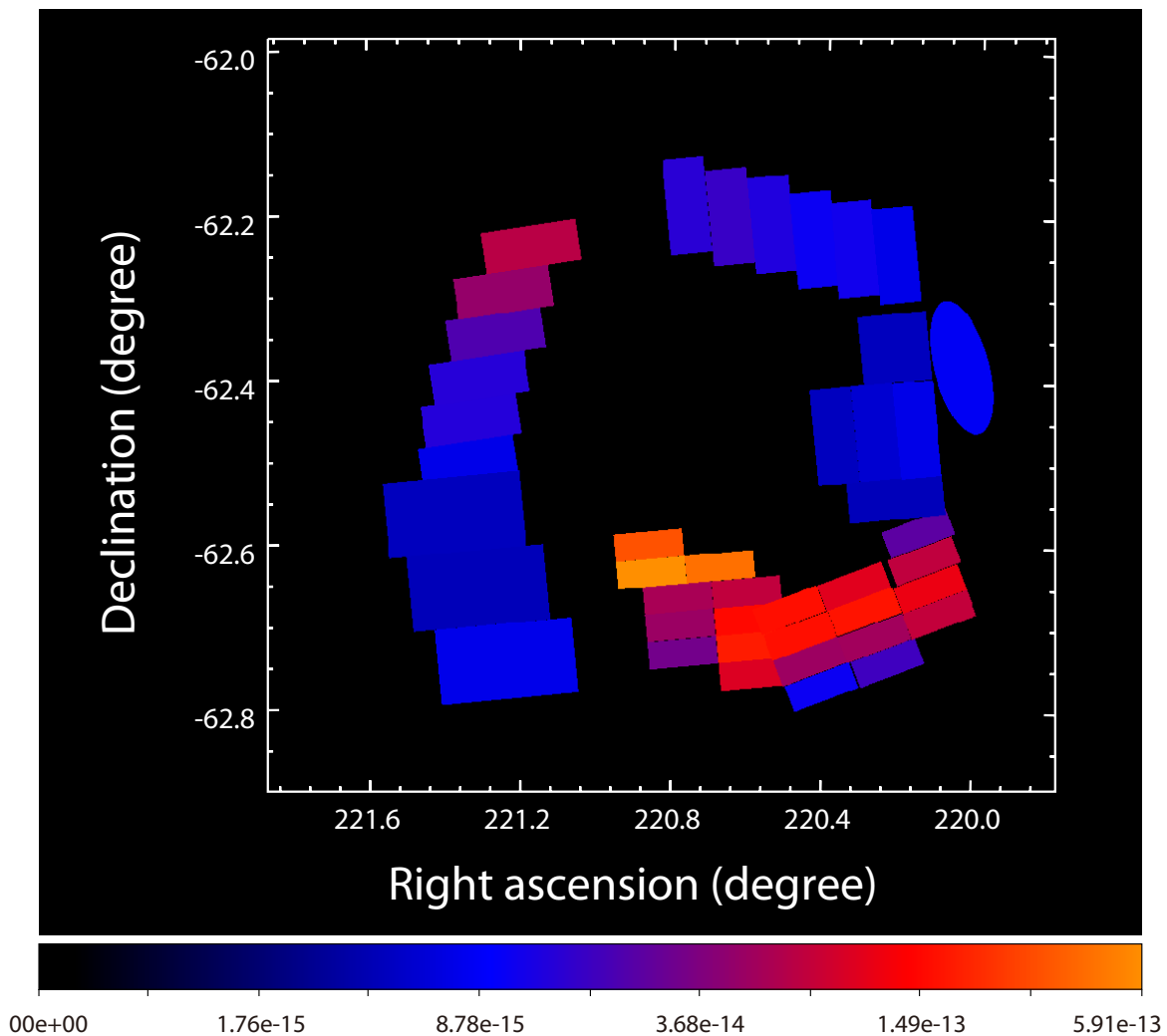


FIG. 5.— The SB_{NT} map. The scale is logarithmic.

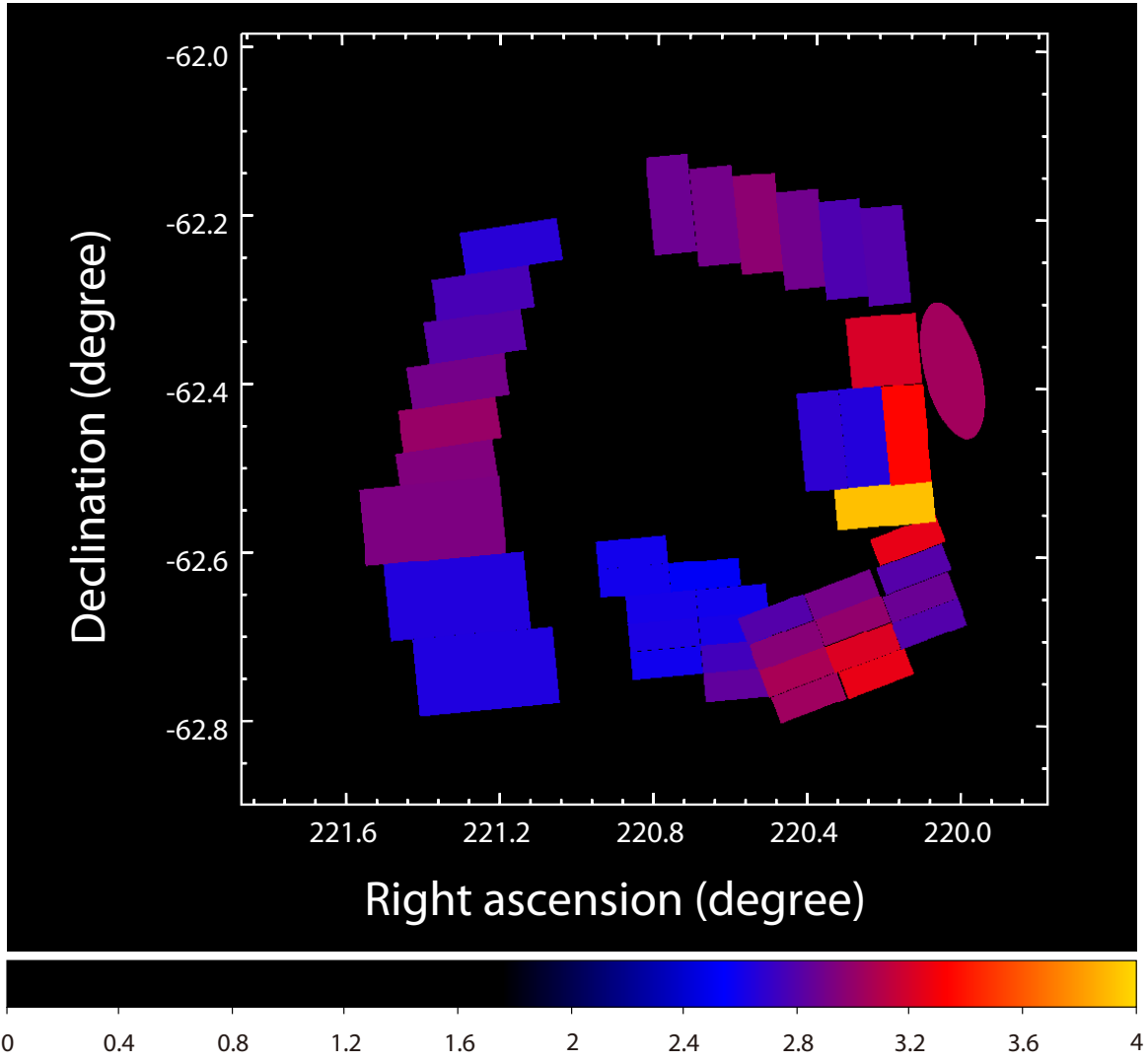


FIG. 6.— The photon index map. The scale is linear.

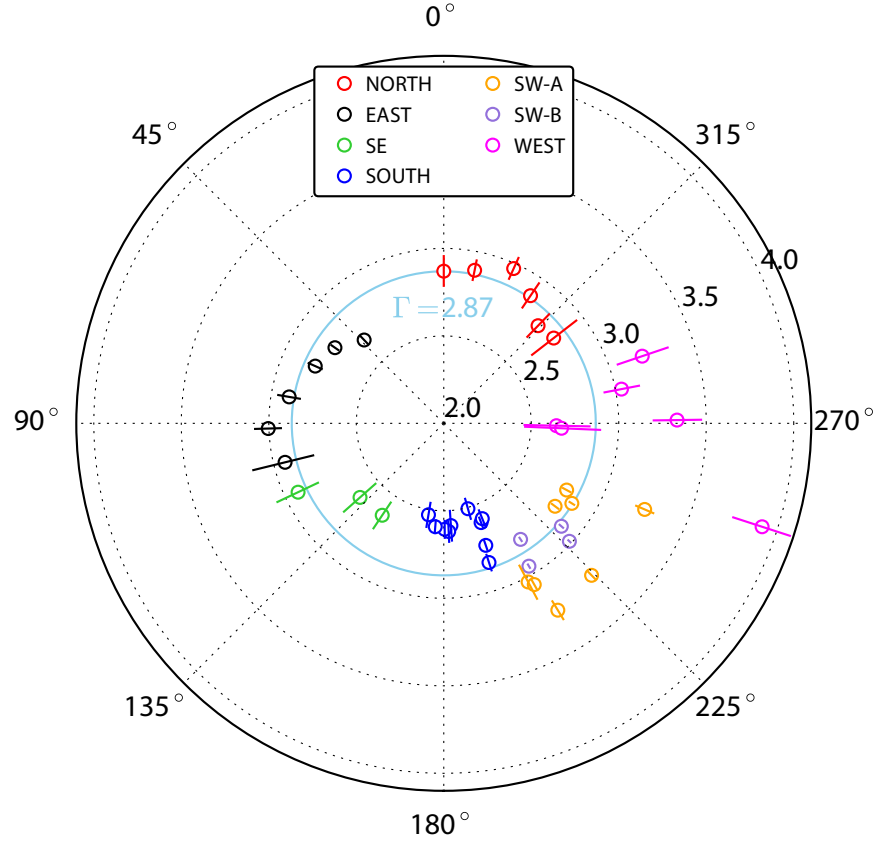


FIG. 7.— The azimuth angle dependence of photon indices. We set NORTH01 to 0° . The cyan line shows the best-fit constant model.

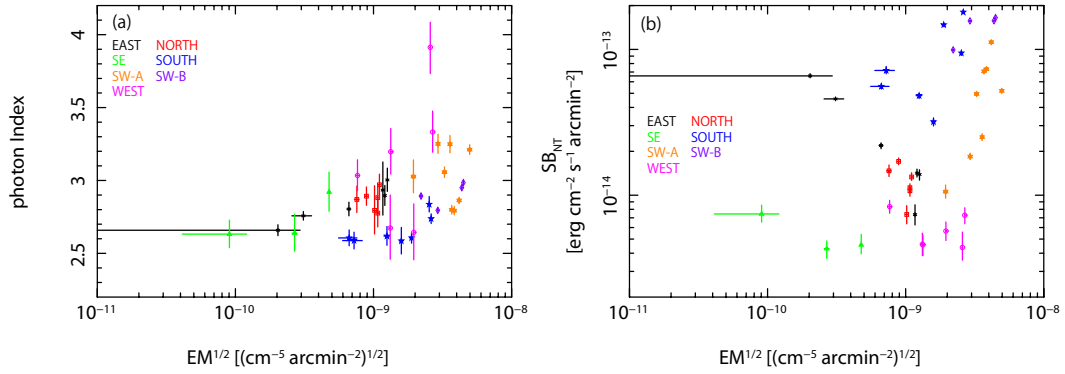


FIG. 8.— (a) Photon indices vs. $EM^{1/2}$, (b) SB_{NT} vs. $EM^{1/2}$.

TABLE 3
THE BEST-FIT PARAMETERS FOR THE SW
REGIONS.

Parameter	SW-A	SW-B
–gsmooth–		
σ (eV at 6 keV)	24 ± 1	30 ± 2
–wabs–		
N_{H} (10^{21} cm^{-2})	3.7 ± 0.1	4.5 ± 0.1
–vpshock–		
kT (keV)	$0.438^{+0.004}_{-0.002}$	0.35 ± 0.01
Ne (solar)	$1.85^{+0.01}_{-0.02}$	1.49 ± 0.05
Mg (solar)	$1.66^{+0.02}_{-0.03}$	1.01 ± 0.07
Si (solar)	$1.62^{+0.04}_{-0.05}$	$1.15^{+0.20}_{-0.18}$
Ca (solar)	1.02 ± 0.01	0.83 ± 0.03
τ ($10^{10} \text{ s cm}^{-3}$)	$6.6^{+0.1}_{-0.2}$	$8.3^{+0.9}_{-0.8}$
Norm (10^{-16} cm^{-5})	8.36 ± 0.02	4.21 ± 0.03
–power-law–		
Γ	3.06 ± 0.01	2.91 ± 0.01
Norm ^a	1.60 ± 0.02	1.85 ± 0.01
–vnei–		
Norm (10^{-21} cm^{-5})	8.9 ± 0.5	5.9 ± 0.4
–gaussian–		
Norm ^b	2.8 ± 1.2	$1.1^{+1.2}_{-1.1}$
–gain–		
slope	1.0032 ± 0.0001	
offset (eV)	-1.5 ± 0.1	
χ^2/dof	2050/905	1557/1026

^a In unit of $10^{-2} \text{ photons keV}^{-1} \text{ s}^{-1} \text{ cm}^{-2}$ at 1 keV.

^b In unit of $10^{-6} \text{ photons s}^{-1} \text{ cm}^{-2}$ in the line.

TABLE 4
THE BEST-FIT PARAMETER FOR ALL EAST REGIONS

Parameter	EAST01	EAST02	EAST03	EAST04	EAST05	EAST06
–vpshock– Norm ^a	2.9±0.1	3.3±0.1	3.1±0.1	0.93±0.06	0.20±0.06	0.06 ^{+0.07} _{–0.06}
–Power-law– Γ	2.9±0.2	3.00±0.08	2.90±0.07	2.80±0.05	2.76±0.03	2.66±0.04
Norm ^b	0.7±0.1	1.4±0.1	1.2±0.1	1.7±0.1	3.4±0.1	3.1±0.1
F _X ^c	1.6 ^{+0.3} _{–0.2}	3.0 ^{+0.2} _{–0.3}	3.0±0.2	4.6±0.2	9.6±0.2	10.1 ^{+0.3} _{–0.2}
–vnei– Norm ^d	<9.9	9.8±4.2	7.5±2.2	<4.4	<0.9	<0.9
χ ² / <i>dof</i>	219/184	304/271	330/285	357/290	468/399	265/250

^a In unit of 10^{–17} cm^{–5}.

^b In unit of 10^{–3} photons keV^{–1} s^{–1} cm^{–2} at 1 keV.

^c In unit of 10^{–13} erg s^{–1} cm^{–2} in the 3.0–5.0 keV band.

^d In unit of 10^{–22} cm^{–5}.

TABLE 5
THE BEST-FIT PARAMETER FOR ALL NORTH REGIONS

Parameter	NORTH01	NORTH02	NORTH03	NORTH04	NORTH05	NORTH06
–vpshock– Norm ^a	1.1±0.1	1.7±0.1	2.6±0.1	2.4±0.1	2.4±0.1	2.2±0.1
–power-law– Γ	2.87±0.09	2.89±0.06	2.97±0.07	2.88±0.09	2.78 ^{+0.10} _{–0.09}	2.8±0.2
Norm ^b	1.1±0.1	1.5±0.1	1.3±0.1	0.9±0.1	0.9±0.1	0.6±0.1
F _X ^c	2.8 ^{+0.3} _{–0.2}	3.6±0.2	2.8±0.2	2.3±0.2	2.4±0.2	1.6±0.2
–vnei– Norm ^d	<6.2	5.1±3.7	3.4±2.8	6.1±3.3	8.9±4.2	<10.3
χ ² / <i>dof</i>	163/133	226/200	200/226	200/190	169/164	160/124

^a In unit of 10^{–17} cm^{–5}.

^b In unit of 10^{–3} photons keV^{–1} s^{–1} cm^{–2} at 1 keV.

^c In unit of 10^{–13} erg s^{–1} cm^{–2} in the 3.0–5.0 keV band.

^d In unit of 10^{–22} cm^{–5}.

TABLE 6
THE BEST-FIT PARAMETER FOR ALL SE REGIONS

Parameter	SE01	SE02	SE03
–vpshock– Norm ^a	1.3±0.1	0.40±0.03	0.05±0.04
–power-law– Γ	2.92 ^{+0.14} _{–0.13}	2.64 ^{+0.13} _{–0.12}	2.63 ^{+0.10} _{–0.09}
Norm ^b	1.1±0.1	0.7±0.1	1.2±0.1
F _X ^c	2.6 ^{+0.5} _{–0.3}	2.4±0.3	4.1 ^{+0.6} _{–0.5}
–vnei– Norm ^d	8.4±6.1	8.0±5.1	<12.2
χ ² / <i>dof</i>	298/259	220/197	204/186

^a In unit of 10^{–17} cm^{–5}.

^b In unit of 10^{–3} photons keV^{–1} s^{–1} cm^{–2} at 1 keV.

^c In unit of 10^{–13} erg s^{–1} cm^{–2} in the 3.0–5.0 keV band.

^d In unit of 10^{–22} cm^{–5}.

TABLE 7
THE BEST-FIT PARAMETER FOR ALL SOUTH REGIONS

Parameter	SOUTH01	SOUTH02	SOUTH03	SOUTH04	SOUTH05
–vpshock– Norm ^a	6.4±0.3	6.8±0.3	3.6±0.2	0.5±0.2	2.5±0.2
–power-law– Γ	2.84±0.05	2.74±0.03	2.61±0.04	2.59±0.06	2.59±0.09
Norm ^b	3.7±0.2	6.2±0.2	4.2±0.1	2.0±0.1	0.9±0.1
F _X ^c	9.5±0.3	18.1 ^{+0.6} _{−0.4}	14.8 ^{+0.3} _{−0.4}	7.2±0.4	3.2±0.2
–vnei– Norm ^d	<2.0	<7.7	<5.1	6.1±5.6	<2.1
χ ² / <i>dof</i>	298/288	445/413	373/352	199/199	195/175
	SOUTH06	SOUTH07	SOUTH08	SOUTH09	SOUTH10
–vpshock– Norm ^a	1.6±0.1	0.4±0.1	<0.05	<0.04	<0.02
–power-law– Γ	2.62 ^{+0.07} _{−0.06}	2.61±0.05	2.51 ^{+0.07} _{−0.06}	2.59±0.04	2.53±0.08
Norm ^b	1.4±0.1	1.6±0.1	1.1±0.1	1.7±0.1	0.8±0.1
F _X ^c	4.8 ^{+0.1} _{−0.2}	5.6±0.2	4.3 ^{+0.2} _{−0.3}	5.9±0.2	3.2±0.2
–vnei– Norm ^d	<3.5	3.8±3.7	<0.9	<1.6	<1.4
χ ² / <i>dof</i>	207/203	208/213	153/156	206/215	148/140

^a In unit of 10^{−17} cm^{−5}.

^b In unit of 10^{−3} photons keV^{−1} s^{−1} cm^{−2} at 1 keV.

^c In unit of 10^{−13} erg s^{−1} cm^{−2} in the 3.0–5.0 keV band.

^d In unit of 10^{−22} cm^{−5}.

TABLE 8
THE BEST-FIT PARAMETER FOR ALL SW-A REGIONS

Parameter	SW01	SW02	SW05	SW06	SW07	SW08	SW09	SW11
–vpshock– Norm ^a	3.8±0.1	10.7±0.1	8.6±0.1	14.8±0.1	17.4±0.1	13.6±0.1	12.8±0.1	24.7±0.1
–power-law– Γ	3.03±0.11	3.06±0.04	3.25±0.07	2.79±0.03	2.86±0.02	2.80±0.03	3.25±0.06	3.21±0.03
Norm ^b	0.5±0.1	2.6±0.1	1.2±0.1	2.7±0.1	4.5±0.1	2.6±0.1	1.7±0.1	3.3±0.1
F _X ^c	1.1±0.1	5.1±0.1	1.9±0.1	7.5±0.2	11.4±0.2	7.2±0.2	2.6±0.1	5.4±0.1
–vnei– Norm ^d	4.5±1.8	11±0.2	9.8±1.9	14±2.3	21±2.8	13±2.3	8.0±1.9	29±2.8
–gaussian– Norm ^e	<11.1	<12.0	<8.4	<3.8	<4.6	<4.9	<8.1	13±6
χ ² / <i>dof</i>	337/280	762/498	978/408	1317/572	1227/690	986/560	764/424	1460/585

^a In unit of 10^{−17} cm^{−5}.

^b In unit of 10^{−3} photons keV^{−1} s^{−1} cm^{−2} at 1 keV.

^c In unit of 10^{−13} erg s^{−1} cm^{−2} in the 3.0–5.0 keV band.

^d In unit of 10^{−22} cm^{−5}.

^e In unit of 10^{−7} photons s^{−1} cm^{−2} in the line.

TABLE 9
THE BEST-FIT PARAMETER FOR ALL SW-B REGIONS

Parameter	SW03	SW04	SW12	SW13
–vpshock– Norm ^a	19.0±0.2	8.6±0.2	20.1±0.2	4.9±0.1
–power-law– Γ	2.95±0.02	2.80±0.02	2.98±0.01	2.89±0.02
Norm ^b	7.2±0.1	5.8±0.1	7.9±0.1	4.2±0.1
F _X ^c	15.8±0.2	15.7±0.2	16.6±0.2	10.0±0.2
–vnei– Norm ^d	17±3.3	4.5±2.8	30±3.3	22±2.8
–gaussian– Norm ^e	<12.7	<4.7	11±8	<11.8
χ ² /dof	917/755	887/716	1059/869	768/677

^a In unit of 10^{−17} cm^{−5}.

^b In unit of 10^{−3} photons keV^{−1} s^{−1} cm^{−2} at 1 keV.

^c In unit of 10^{−13} erg s^{−1} cm^{−2} in the 3.0–5.0 keV band.

^d In unit of 10^{−22} cm^{−5}.

^e In unit of 10^{−7} photons s^{−1} cm^{−2} in the line.

TABLE 10
THE BEST-FIT PARAMETER FOR ALL WEST REGIONS

Parameter	WEST01	WEST02	WEST03	WEST04	WEST05	WEST06
–vpshock– Norm ^a	14.0±0.2	15.1±0.2	8.0±0.1	3.7±0.1	4.5±0.1	1.8±0.1
–power-law– Γ	3.9±0.2	3.3±0.1	2.6±0.2	2.7±0.2	3.2±0.2	3.0±0.1
Norm ^b	1.5±0.2	1.2±0.1	0.4±0.1	0.3±0.1	0.7±0.1	1.3±0.1
F _X ^c	1.1 ^{+0.3} _{−0.2}	1.7±0.2	1.3±0.2	1.0±0.2	1.2±0.2	2.6±0.3
–vnei– Norm ^d	13±5.5	8.0±3.7	12±3.3	13±3.7	8.9±3.3	<6.1
χ ² /dof	510/243	452/281	307/233	205/164	275/208	231/182

^a In unit of 10^{−17} cm^{−5}.

^b In unit of 10^{−3} photons keV^{−1} s^{−1} cm^{−2} at 1 keV.

^c In unit of 10^{−13} erg s^{−1} cm^{−2} in the 3.0–5.0 keV band.

^d In unit of 10^{−22} cm^{−5}.